Molecular Modeling of Combustion Kinetics. The Abstraction of Primary and Secondary Hydrogens by Hydroxyl Radical

Wei-Ping Hu, Ivan Rossi, Jose C. Corchado,† and Donald G. Truhlar*

Department of Chemistry and Supercomputer Institute, University of Minnesota, Minneapolis, Minnesota 55455

Received: January 13, 1997; In Final Form: June 27, 1997[⊗]

We present a simulation of the combustion reaction OH + propane using variational transition-state theory, multidimensional semiclassical tunneling calculations, and a dual-level approach to direct dynamics as a way to interface dynamical theory with electronic structure theory. The propane reaction involves new features as compared to the simpler reactions that have been simulated previously; in particular three unique transition states are involved—two involving hydroxyl attack at the primary carbon and one involving attack at the secondary carbon. Optimizing the transition state with scaled electron correlation is found to have only a small effect on the geometry but gives improved barrier heights that are only 0.4−0.7 kcal above our best estimates. Combining the three transition state structures with five different isotopic substitution patterns that have been considered experimentally leads to 22 unique reaction processes, for all of which we calculate the reaction rate by dual-level direct dynamics with an empirically scaled barrier height. The results confirm the assumptions used by experimentalists that primary and secondary site reaction rate constants are almost the same in different isotopic environments. The calculations show that the experimentally measured kinetic isotope effects are dominated by tunneling effects.

1. Introduction

The application of variational transition-state theory[1−3] (VTST) and semiclassical tunneling methods[2,3] to dynamical calculations requires an accurate knowledge of the potential energy surface.[4] For organic reactions, the calculation of a complete and accurate potential energy surface is prohibitive because of the size of the systems. In recent papers,[5−14] several methods have been developed to carry out this kind of calculation more economically. The dual-level (or VTST-IC) dynamics method[11,12] has been shown to be a powerful tool for reaction-path dynamics calculations of polyatomic systems, but the necessity of carrying out high-level calculations on the stationary points makes the study of large systems still very challenging.

In the present paper we have applied the dual-level approach to the hydrogen abstraction reactions of propane and its isotopic derivatives by hydroxyl radical. The large size of this system restricts the level of the electronic structure theory that can be used for the high level for this system. One partial solution is to scale the correlation energy by means of the scaling-all-correlation (SAC) method,[15] and in this paper we employ the MP2−SAC method. In this method, one uses the experimental,[16] Hartree−Fock (HF),[17] and Møller−Plesset second-order perturbation theory (MP2)[17] dissociation energies to obtain scaling factors for the correlation energy in order to reproduce the experimental energy of reaction for the two half-reactions of the reaction under study. In the present case these half-reactions are $C_3H_8 \rightarrow C_3H_7 + H$ and $H + OH \rightarrow H_2O$. By applying an average scaling factor, or by modifying the basis sets to obtain the same scaling factors for the two half reactions, the correlation energy of the saddle point can then be scaled, and one can expect to obtain a better estimate of the barrier height. Since the scaling factor in the SAC method is calibrated to experimental data, it corrects for the incompleteness of the basis set and the lack of full configuration interaction, thereby allowing one to improve the accuracy over conventional MP2 calculations with negligible additional cost.

In hydrocarbon combustion and other oxidation reactions of hydrocarbons, one of the important rate-determining steps is the abstraction of a hydrogen atom by the hydroxyl radical. In the case of propane, the hydrogen can be abstracted from two chemically different classes of hydrogens atoms, i.e., from the two terminal methyl groups or from the middle methylene group. In studying the kinetic isotope effects, protium atoms in either or both of the classes may be replaced by deuteriums. As shown by Droege and Tully,[18] this makes six distinct reactions in terms of reactants, and there are 14 possible sets of products. However, the three hydrogens in the methyl group are not chemically equivalent in the equilibrium structure, and there are two different ways they can be abstracted. Thus, in terms of geometry, there are three distinct transition states corresponding to different abstraction sites in the hydrogen abstraction reactions of propane by the hydroxyl radical, and there are in total 22 different elementary reactions involved. Within the Born−Oppenheimer approximation, the transition states for the deuterium-substituted reactions are geometrically the same.

In ref 18 the authors measured the rate constants of perprotiopropane and five labeled isotopically propanes. For reference we note that the six reactions are

R1: $OH + C_3H_8$

R2: $OH + CH_3CD_2CH_3$

R3: $OH + CD_3CH_2CH_3$

R4: $OH + CD_3CD_2CH_3$

R5: $OH + CD_3CH_2CD_3$

R6: $OH + C_3D_8$

where in each case the rate constant refers to overall loss of

† Visiting scientist, Spring 1994 and 1996 to present. Permanent address: Departamento de Quimica-Fisica, Universidad de Extremadura, 06071-Badajoz, Spain.

[⊗] Abstract published in *Advance ACS Abstracts,* August 15, 1997.

S1089-5639(97)00188-6 CCC: $14.00

hydroxyl radical by abstraction of H or D. By assuming separability of the abstraction sites and using predetermined values[19] (based on the OH + C_2H_6 reaction) of the kinetic isotope effect for primary abstraction, Droege and Tully[18] were able to deduce the abstraction rate constants at the two different (primary and secondary) sites for hydrogen and deuterium abstractions. In this paper, we study the elementary reactions corresponding to the 22 distinct reaction paths separately, and we calculate the rate constant of each individual reaction. The results are then used to check the abstraction site separability assumption and to understand various dynamical properties of these reactions.

In this paper the numbering scheme for the reactions is as follows. The six reactions in ref 18 are labeled R = 1, 2, ..., 6; the two elementary reactions corresponding to the two primary hydrogen abstraction sites are labeled R.1 for the abstracted atom trans to the methyl group and R.2 for the abstracted atom gauche to the methyl group; and the secondary hydrogen abstraction reaction is labeled as R.3. These labels are further followed by either (H) or (D) which specifies that a hydrogen or a deuterium is being abstracted. For example, in (R2) the abstractions of the primary hydrogens are labeled as 2.1 (H) and 2.2 (H), and the abstraction of the secondary hydrogens is labeled as 2.3 (D).

2. Computational Methods

In this work, all 22 reaction rates were calculated by the dual-level dynamics method[11] in which the high-level data were obtained by correlated electronic structure calculations employing the MP2−SAC[16] method. The theoretical basis for the SAC method is explained elsewhere.[15,20]

Structure. To use the SAC method for this reaction, one needs to obtain similar scaling factors, called F_2, with the same basis set for three bond dissociation reactions, i.e., the O−H bond in water, the primary (terminal) C−H bond, and the secondary (middle) C−H bond in propane. We started with Dunning's augmented correlation-consistent polarized valence double-ζ (aug-cc-pVDZ) basis set,[21,22] for which the whole system contains 173 contracted basis functions and 300 primitive Gaussian functions. We found that the F_2 values for the three bond dissociation energies are 0.922, 0.869, and 0.884, respectively, at the MP2/aug-cc-pVDZ level. We concluded that modifications to the basis set are needed to balance the basis set for these reactions.

We made three changes to the starting basis set, based on the strategy of changing only polarization functions, since this is less likely to unbalance the change distribution than changing valence functions. (1) For oxygen, we changed the exponent of the d polarization function from 1.185 to 0.635. (2) For all carbons, we replaced the aug-cc-pVDZ basis set by the triple-ζ cc-pVTZ basis set[21] without the *f* function. (3) For the central carbon we increased the cc-pVTZ basis set with one extra p function with exponent 1.200. The original aug-cc-pVDZ basis set is still used for the hydrogens. We call this new basis set BTZ (balanced triple-ζ), which is a correct description since each C or O contains three noncore s and p shells, and each H contains three s shells. We also note that the polarized space of the BTZ basis is (2d,2p), i.e., each C and O contains two d shells, and each H contains two p shells. With the BTZ basis set the whole system contains 176 contracted basis functions and 318 primitive Gaussian functions, and we obtain an F_2 value of 0.895 for all three bond dissociation energies. We then use the new basis set to obtain the optimized geometries and energies of the reactants, products, and saddle points at the MP2−SAC level. The calculated geometry for the reactants, products, and the transition states are depicted in Figures 1−6. More detailed information about geometries is included in the Supporting Information. The vibrational frequency calculations were performed at the MP2/aug-cc-pVDZ level (at the optimized geometries of the same level, of course).

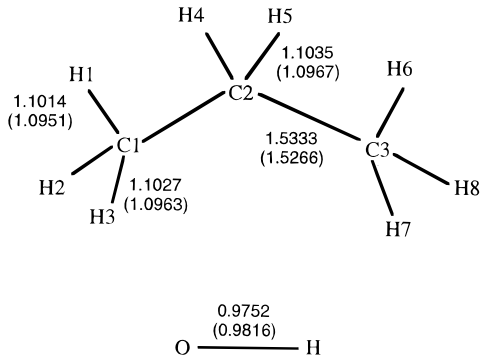

Figure 1. Bond lengths in angstroms for the reactants at the MP2/aug-cc-pVDZ level. The values in parentheses are the MP2−SAC/BTZ results. The bond angles ∠C1−C2−C3 = 112.1° (111.8°), ∠C2−C1−H1 = 111.7° (111.8°), ∠C2−C1−H3 = 110.8° (110.7°), ∠C1−C2−H4 = 109.5° (109.6°), and the dihedral angel ∠H1−C1−C2−H4 = −58.3° (−58.2°).

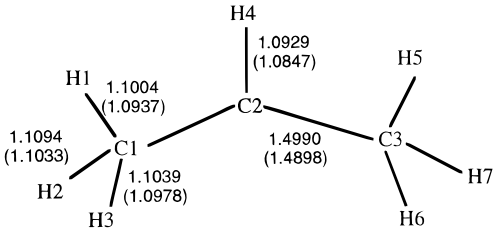

Figure 2. Bond lengths in angstroms for the isopropyl radical at the MP2/aug-cc-pVDZ level. The values in parentheses are the MP2−SAC/BTZ results. The bond angles ∠C1−C2−C3 = 119.7° (119.5°), ∠C2−C1−H1 = 111.9° (112.1°), ∠C2−C1−H2 = 111.5° (111.4°), ∠C2−C1−H3 = 111.0° (111.1°), ∠C1−C2−H4 = 118.7° (119.1°), and the dihedral angel ∠H1−C1−C2−H4 = −29.4° (−26.0°).

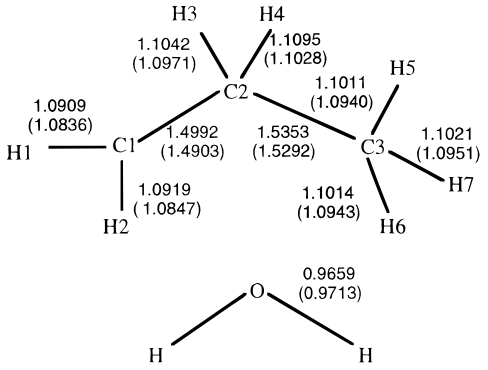

Figure 3. Bond lengths in angstroms for the *n*-propyl radical and water at the MP2/aug-cc-pVDZ level. The values in parentheses are the MP2−SAC/BTZ results. The bond angles ∠C1−C2−C3 = 112.8° (112.7°), ∠C2−C1−H1 = 121.1° (121.0°), ∠C2−C1−H2 = 120.4° (120.1°), ∠C1−C2−H3 = 109.7° (109.7°), ∠C1−C2−H4 = 109.8° (109.9°), ∠C2−C3−H5 = 111.3° (111.4°), ∠C2−C3−H6 = 110.8° (110.8°), ∠C2−C3−H7 = 110.6° (110.6°), and the dihedral angel ∠H1−C1−C2−H3 = 39.4° (38.8°), ∠H5−C3−C2−H3 = −58.4° (−58.3°). For water, ∠H−O−H = 103.9° (104.1°).

Our lower level of electronic structure theory for the dual-level direct dynamics calculations is semiempirical molecular orbital theory with neglect of diatomic differential overlap[23−25] (NDDO). Although general parametrizations of NDDO theories are sometimes employed directly to study of OH abstraction reactions,[26] their quantitative accuracy is not reliable. The low-

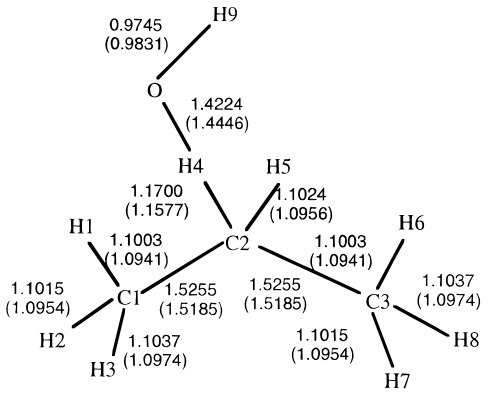

Figure 4. Bond lengths in angstroms for the secondary-site transition state at the MP2/aug-cc-pVDZ level. The values in parentheses are the MP2−SAC/BTZ results. The bond angles ∠C1−C2−C3 = 114.2° (113.9°), ∠C1−C2−H4 = 106.8° (107.0°), ∠C1−C2−H5 = 111.5° (111.5°), ∠C2−H4−O = 176.7° (175.6°), ∠H4−O−H9 = 95.6° (95.3°), and the dihedral angel ∠H1−C1−C2−H4 = −59.7° (−59.6°), ∠H9−O−H4−C2 = 0.0° (0.1°).

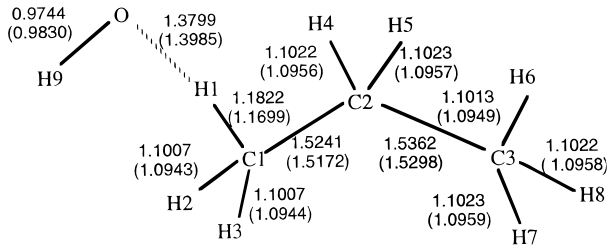

Figure 5. Bond lengths in angstroms for the trans primary-site transition state at the MP2/aug-cc-pVDZ level. The values in parentheses are the MP2−SAC/BTZ results. The bond angles ∠C1−C2−C3 = 111.6° (111.3°), ∠C2−C1−H1 = 108.3° (108.0°), ∠C1−H1−O = 171.6° (174.7°), ∠H1−O−H9 = 96.5° (96.2°), and the dihedral angel ∠H1−C1−C2−H4 = −59.7° (−59.2°), ∠H9−O−C1−H2 = 1.9° (29.6°).

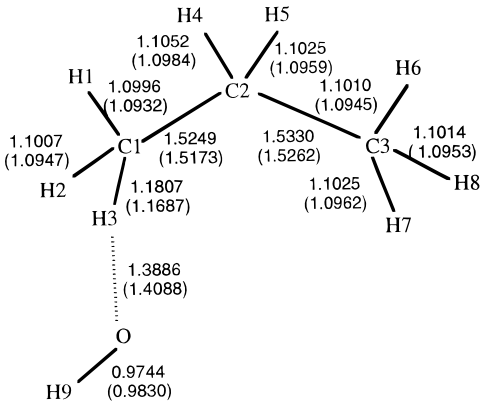

Figure 6. Bond lengths in angstroms for the gauche primary-site state at the MP2/aug-cc-pVDZ level. The values in parentheses are the MP2−SAC/BTZ results. The bond lengths are in angstroms. The bond angles ∠C1−C2−C3 = 111.9° (111.5°), ∠C2−C1−H3 = 106.5° (106.6°), ∠C1−H3−O = 174.4° (171.9°), ∠H3−O−H9 = 96.0° (95.7°), and the dihedral angel ∠H3−C1−C2−H4 = −179.2° (−179.9°), ∠H9−O−C1−H1 = 28.9° (21.4°).

level data were therefore obtained using the AM1−SRP[5] semiempirical method. The original AM1[24] and PM3[25] methods predict energies of reaction differing by 5−13 kcal/mol from the experimental values, and they predict barrier heights 3−7 kcal/mol higher than the MP2−SAC values. The imaginary vibrational frequencies of the transition states calculated from the PM3 methods are very different from the MP2 values, and this could have a deleterious effect on the barrier width in the resulting VTST-IC implicit potential function. Thus the AM1 method is chosen as a starting point for the parameter adjustment in the specific reaction parameters (SRP)[5,6,8,11−14,27] method. A genetic algorithm[28] (GA) was applied to search the parameter space of the AM1 method to obtain a new set of parameters that predict a much better energy of reaction and barrier height for each reaction.

TABLE 1: Changed Parameters (in eV) in AM1SRP Method

	primary-site reaction	secondary-sige reaction
U_{ss}(H)	11.461 394	11.304 162
U_{ss}(C)	55.840 785	54.783 060
U_{ss}(O)	102.471 055	102.519 970
U_{pp}(C)	37.640 103	37.659 910
U_{pp}(O)	79.711 799	80.007 705
β_s(H)	6.426 086	6.468 292
β_s(C)	16.475 327	16.483 185
β_s(O)	28.325 732	27.775 998
β_p(C)	8.086 839	8.130 484
β_p(O)	28.170 090	27.957 288

TABLE 2: Calculated Imaginary Frequencies (in cm^{-1}) of the Transition States

level	trans primary site	gauche primary site	secondary site
PM3	2472*i*	2493*i*	2552*i*
AM1	1683*i*	1708*i*	1637*i*
AM1−SRP	1079*i*	1118*i*	924*i*
MP2/aug-cc-pVDZ	1388*i*	1322*i*	975*i*

In each SRP parameter optimization, a subset of parameters is allowed to change within a prescribed tolerance of their original values and their values are optimized by the GA. The unfitness criterion minimized by the GA is a sum of the following terms: (1) absolute differences between reference and predicted forward barriers; (2) absolute differences between reference and predicted exothermicities; (3) a standard penalty for each geometry optimization that is not completely converged. Barriers and exothermicities are weighted the same.

We decided to optimize the geometries at every step of the GA because we have too few points to use the same approach as in our applications[28] to Cl + CH_4. This allows us to use the real energy differences between the stationary points instead of approximated ones in the unfitness. Therefore, for each trial parameter set generated by the GA (i.e., for each population member in each generation) the geometries of all the stationary points are optimized using the EF algorithm.[29] If any activation barrier is negative or if any energy is not converged, then the unfitness of the parameter set is given a very high value.

We also generated a parameter set where even the imaginary frequencies were taken into account in the penalty function, but the errors in the energies were larger than for the best AM1−SRP set. We chose final parameters on the basis of the resulting reaction energetics and shape of the potential along the minimum energy path (i.e., we wanted a simple barrier shape without spurious wells). We used different SRP parameter sets for the primary site and the secondary site in order to make the low-level surface of the dual-level approach as accurate as possible in each case. The parameters changed from the original values in the AM1−SRP calculations are listed in Table 1. The imaginary frequencies of the transition states calculated at different levels of theory are compared in Table 2.

It is interesting to compare the bond lengths of the making and breaking bonds at the AM1, AM1−SRP, and SAC optimized structures for the three transition states. For the breaking C−H bond, AM1 yields 1.21 Å, AM1−SRP yields 1.20−1.21 Å, and MP2−SAC yields 1.16−1.17 Å. For the

TABLE 3: Levels of Dynamical Theory

physical effect on rate	TST	CVT	CVT/μOMT
include contribution of vibrations and rotations to activation energy?	yes	yes	yes
include variation of vibrations and rotations along reaction path in determining location of transition state?	no	yes	yes
include tunneling?	no	no	yes

making O−H bond, AM1 yields 1.38−1.41 Å, AM1−SRP yields 1.44−1.47 Å, and MP2−SAC yields 1.40−1.44 Å. The average absolute deviation of transition state frequencies from our best ab initio values is about 10% for both AM1 and AM1−SRP. Thus the geometries and frequencies are not improved as much, if any, as the energies.

The new AM1−SRP surfaces then serve as the low-level potential energy function for all dual-level dynamics calculations. According to the naming convention in ref 11, the dual-level dynamics scheme that has just been described may be designated as MP2−SAC/BTZ[MP2/aug-cc-pVDZ]///AM1−SRP, where the notation "///" is used to denote "with the reaction path calculated by" (analogous to "//" which is widely used[17] to denote "with the stationary point geometries optimized by") and where the brackets specify the level used for a Hessian when it is lower than the highest level used for geometry optimization.

Dynamical Theory. The level of variational transition-state theory used in this study is canonical variational theory[1−3,30] (CVT), and the level of tunneling calculation employed is the microcanonical optimized multidimensional tunneling method[8] (μOMT). When the CVT method is employed without the tunneling corrections, it is just called CVT, whereas when tunneling is added it is called CVT/μOMT. These are both examples of variational transition-state theory (VTST). In a few cases we also present results obtained by conventional (TST). When tunneling is included, we also always include nonclassical reflection[31] at energies above the barrier; thus "tunneling" is really a shorthand notation for "quantum effects on reaction-coordinate motion". The essential elements of the three levels of dynamical theory employed are summarized in Table 3.

Dynamical Methods. The first step for each reaction is to calculate the reaction path as well as geometries, energies, gradients, and Hessians as a function of the reaction coordinate s by the low-level method. These primary electronic structure data are used to calculate the moment of inertia for overall rotation, reduced moments of inertia for internal rotation, reaction-path curvature vectors, and generalized-normal-mode vibrational frequencies and eigenvectors, all as a function of s. The rotational moments of inertia are obtained from the optimized geometry at the MP2/aug-cc-pVDZ level, and energies and moments of inertia along the reaction path are corrected to the higher level by the VTST-IC algorithm.[11] All vibrational modes other than the lowest-frequency one are treated harmonically, and the lowest-frequency one is treated as a hindered internal rotator as discussed below. There are 32 vibrational modes orthogonal to the reaction path. The 28 largest frequencies are calculated as a function of s by the dual-level VTST-IC method.[11] The four lowest frequencies are calculated as a function of s by the single-level IVTST-0 method,[7] using high-level data at the three stationary points along the reaction path.

The lowest-frequency mode of each generalized transition state is treated by a modified version of the original[8,32,33] hindered rotor approximation. The modification is a general technique that could be used for a variety of applications, and it is based on using an estimated rotational barrier. In the original formulation of the hindered rotor approximation, the partition function for mode m treated as a hindered rotor is approximated as

$$Q_m^{\mathrm{hin}} = Q_m^{\mathrm{har}} \tanh Q_m^{\mathrm{fr}} u_m \tag{1}$$

where Q_m^{har} and Q_m^{fr} are the harmonic and free-rotor partition functions and u_m is a reduced frequency.[32] This has the correct limits

$$Q_m^{\mathrm{hin}} \xrightarrow{T \to 0} Q_m^{\mathrm{har}} \tag{2}$$

$$Q_m^{\mathrm{hin}} \xrightarrow{T \to \infty} Q_m^{\mathrm{fr}} \tag{3}$$

and the rate at which the transition occurs is controlled by u_m, which is

$$u_m = \hbar\omega_m/\tilde{k}T \tag{4}$$

where ω_m is the frequency in s^{-1} of mode m calculated from the second derivative at the minimum of the potential for internal rotation, $\tilde{k}$ is Boltzmann's constant, and T is temperature. This corresponds to approximating the hindered rotor potential as

$$V = V_0 + {}^1/_2 W_m(1 - \cos \sigma_m \phi) \tag{5}$$

where the internal rotational barrier is

$$W_m = 2\omega_m{}^2 \bar{I}_m \tag{6}$$

This is presumably a good approximation to the low-energy part of the potential, near $V = V_0$, but a less valid approximation to the high-energy part. In particular it sometimes predicts an unreasonably high internal rotational barrier. A more valid high-energy approximation, valid near $V = V_0 + W_m$, would be to set W_m equal to the actual barrier height to internal rotation. Call this actual barrier height W_m^{HT}, and calculate an effective high-temperature frequency by

$$\omega_m^{\mathrm{HT}} = (W_m^{\mathrm{HT}}/2\bar{I}_m)^{1/2} \tag{7}$$

Thus we write an effective frequency as

$$\omega_{\mathrm{m}}^{\mathrm{eff}} = \omega_m + (\omega_m^{\mathrm{HT}} - \omega_m^{\mathrm{LT}}) G_m(T) \tag{8}$$

where

$$G_m(T) = \begin{cases} g_m(T)/Wm^{\mathrm{HT}} & g_m(T) \le W^{\mathrm{HT}} \\ 1 & g_m(T) \ge W^{\mathrm{HT}} \end{cases} \tag{9}$$

and

$$g_m(T) = \max \begin{cases} \tilde{k}T \\ {}^1/_2 \hbar\omega_m \end{cases} \tag{10}$$

We use (8) in both Q_m^{har} and u_m in eq 1 based on ab initio values of W_m^{HT} that are discussed section 4. In particular the u_m in eq 1 is replaced by

$$u_m = \hbar\omega_{m,eff}/kT \tag{11}$$

This effectively further lowers the estimated hindered-rotor partition function at higher temperatures.

TABLE 4: Classical Energy of Reaction (in kcal/mol) Calculated at Different Levels of Theory Compared to Experiment[a]

	n-propyl	isopropyl
PM3	−23.5	−30.6
AM1	−26.8	−32.3
AM1−SRP	−18.4	−20.8
MP2/aug-cc-pVDZ	−18.4	−20.6
MP2-SAC/BTZ	−18.2	−20.8
QCISD(T)//MP2/aug-cc-pVDZ	−14.5	−16.8
experiment[b]	−18.6	−19.6

[a] Excluding zero-point energies in both theoretical and experimental values. [b] From ref 16.

TABLE 5: Classical Barrier Height (in kcal/mol) Calculated at Different Levels of Theory

	primary site 1[a]	primary site 2[b]	secondary site
PM3	8.3	7.7	6.0
AM1	10.3	9.9	9.4
AM1−SRP	4.0	3.9	2.6
MP2/aug-cc-pVCZ	5.8	5.3	3.9
MP2-SAC/BTZ	4.4	3.8	2.6
QCISD(T)/aug-cc-pVDZ// MP2/aug-cc-pVDZ	3.4	3.0	1.4
SB-MP2-SAC/BTZ[c]	3.7	3.2	2.2

[a] In plane. [b] Out of plane. [c] This row incorporates an empirical scale factor of 0.85.

The reduced moment of inertia was calculated as explained elsewhere[8,32,33] with the assumption that the two subsystems rotating with respect to each other are HO and HC_2H_5, and the symmetry number for hindered internal rotation is taken as 1.0.

We assume that the electronic excitation energies and degeneracies of the generalized transition states are the same as those of the conventional transition state, and we assume no low-lying excited electronic states of the $^2A'$ saddle point; therefore the electronic partition function of all conventional and generalized transition states is 2. We include the $^2\Pi_{1/2}$ excited state of OH (and OD) in the reactant electronic partition function, and we use the experimental value,[34] 140 cm^{-1}, for the $^2\Pi_{1/2}$ excitation energy.

The scaling mass[2,30] μ for mass-scaled coordinates was set equal to 1 amu. The first step off the saddle point was taken in the direction of the imaginary-frequency normal mode of the saddle point, and the rest of the reaction path was calculated by the Euler one-step method[2] with a step size of 0.002 a_0. Hessians were calculated at intervals of 0.01 or 0.02 a_0, depending on the reaction.

Final Scaling. The energies of reaction calculated at different levels of theory are compared to the experimental values for both reactions in Table 4. The calculated classical barrier heights for the three abstraction sites at different levels of theory are shown in Table 5. First we carried out calculations using the MP2−SAC/BTZ results as the higher level, as described in section 2. We found, however, that rate constants calculated that way are consistently lower than the experimental values. We conclude that the correlation energies are still not fully recovered at the transition states even with the SAC method. Thus, as a final adjustment to the simulation model, we scaled the barrier height by a factor of λ, using the same factor for all three transition states (gauche primary, trans primary, and secondary). We used MP2−SAC/BTZ///AM1−SRP calculations to find an empirical value of λ by comparing to experimental rate constants and finally settled on $\lambda = 0.85$. The use of scaled barriers is denoted SB. Since the classical energies of the high-level calculations at the saddle points are scaled with respect to reactants by a factor of 0.85, and since the MP2−SAC/BTZ energies of reaction are employed without change, the barrier heights for the backward reactions also decrease.

TABLE 6: Calculated Rate Constants (in cm^3 $molecule^{-1}$ s^{-1}) for the First Primary-Site Hydrogen Abstraction Reaction

T (K)	$k_{1.1}$(H)	$k_{2.1}$(H)	$k_{3.1}$(H)	$k_{4.1}$(H)
295.0	5.35*E*−14	6.60*E*−14	5.14*E*−14	6.19*E*−14
342.0	8.35*E*−14	9.75*E*−14	8.20*E*−14	9.64*E*−14
351.5	9.05*E*−14	1.05*E*−13	8.91*E*−14	1.04*E*−13
428.0	1.59*E*−13	1.78*E*−13	1.60*E*−13	1.82*E*−13
437.2	1.68*E*−13	1.88*E*−13	1.70*E*−13	1.93*E*−13
505.0	2.45*E*−13	2.76*E*−13	2.57*E*−13	2.69*E*−13
603.0	3.96*E*−13	4.39*E*−13	4.22*E*−13	4.34*E*−13
728.0	6.60*E*−13	7.20*E*−13	6.47*E*−13	6.69*E*−13
854.0	1.02*E*−12	1.02*E*−12	1.00*E*−12	1.03*E*−12

[a] In the tables, *E*−14 denotes $\times 10^{-14}$.

Software and Hardware. The ab initio electronic structure calculations were performed using the Gaussian 92 program[35] on Cray C90 and Cray X-MP-EA computers at Minnesota Supercomputer Institute. Gaussian 92 was modified locally in order to carry out optimizations at the MP2−SAC level. The AM1, PM3, and AM1−SRP calculations were carried out with a locally modified version of the MOPAC program.[36] The dynamics calculations were performed using the Morate version 6.3 program[37] on a Cray C90 computer.

3. Results for Rate Constants, Kinetic Isotope Effects, and Branching Percentages

The symmetry number for each reaction is the number of protium or deuterium atoms at the given abstraction site. For example, for reactions 1.1, 1.2, and 1.3 the symmetry numbers are 2 (trans), 4 (gauche), and 2 (secondary), respectively. To see the site dependence of individual reaction events more clearly, though we define $k_{R.1}$, $k_{R.2}$, and $k_{R.3}$ without symmetry numbers, i.e., on a per-hydrogen-atom basis. Tables 6−11 list the calculated rate constants on such a per-hydrogen-atom basis for the 22 reactions. These calculations are all carried out at the CVT/μOMT dynamical level and the SB-MP2−SAC/BTZ-[MP2/aug-ccpVDZ]///AM1−SRP electronic structure level. In the notation introduced above, we have

$$k_1 = 2k_{1.1}(\mathrm{H}) + 4k_{1.2}(\mathrm{H}) + 2k_{1.3}(\mathrm{H}) \quad (12)$$

$$k_2 = 2k_{2.1}(\mathrm{H}) + 4k_{2.2}(\mathrm{H}) + 2k_{2.3}(\mathrm{D}) \quad (13)$$

$$k_3 = 1k_{3.1}(\mathrm{H}) + 1k_{3.1}(\mathrm{D}) + 2k_{3.2}(\mathrm{H}) + 2k_{3.2}(\mathrm{D}) + 2k_{3.3}(\mathrm{H}) \quad (14)$$

$$k_4 = 1k_{4.1}(\mathrm{H}) + 1k_{4.1}(\mathrm{D}) + 2k_{4.2}(\mathrm{H}) + 2k_{4.2}(\mathrm{D}) + 2k_{4.3}(\mathrm{D}) \quad (15)$$

$$k_5 = 2k_{5.1}(\mathrm{D}) + 4k_{5.2}(\mathrm{D}) + 2k_{5.3}(\mathrm{H}) \quad (16)$$

$$k_6 = 2k_{6.1}(\mathrm{D}) + 4k_{6.2}(\mathrm{D}) + 2k_{6.3}(\mathrm{D}) \quad (17)$$

Table 12 and Figures 7−12 show the comparison of the calculated observable rate contants to the experimental values at different temperatures, and Tables 13 and 14 present calculated KIEs and branching percentages. Tables 15−17 show the KIEs calculated with TST, CVT, and CVT/μOMT rate constants of the perprotic and the perdeuterated reactions.

We calculated average values of the primary and secondary abstraction rate constants as unweighted averages of the individual primary-site and secondary-site rate constants for both H and D. For example, the average secondary site rate for H

TABLE 7: Calculated Rate Constants (in cm^3 molecule^{-1} s^{-1}) for the First Primary-Site Deuterium Abstract Reaction

T (K)	$k_{3.1}$(D)	$k_{4.1}$(D)	$k_{5.1}$(D)	$k_{6.1}$(D)
295.0	8.17E−15	8.10E−15	7.65E−15	8.15E−15
351.5	1.85E−14	1.84E−14	1.77E−14	1.85E−14
437.2	4.73E−14	4.60E−14	4.45E−14	4.63E−14
505.0	8.46E−14	8.24E−14	8.05E−14	8.30E−14
603.0	1.67E−13	1.62E−13	1.60E−13	1.63E−13
728.0	3.29E−13	3.21E−13	3.15E−13	3.21E−13
854.0	5.69E−13	5.56E−13	5.40E−13	5.55E−13

TABLE 8: Calculated Rate Constants (in cm^3 molecule^{-1} s^{-1}) for the Second Primary-Site Hydrogen Abstraction Reaction

T (K)	$k_{1.2}$(H)	$k_{2.2}$(H)	$k_{3.2}$(H)	$k_{4.2}$(H)
295.0	6.15E−14	6.30E−14	6.15E−14	6.20E−14
351.5	9.40E−14	9.55E−14	9.20E−14	9.25E−14
437.2	1.57E−13	1.61E−13	1.51E−13	1.50E−13
505.0	2.23E−13	2.25E−13	2.11E−13	2.11E−13
603.0	3.37E−13	3.33E−13	3.23E−13	3.25E−13
728.0	5.12E−13	5.20E−13	5.15E−13	5.15E−13
854.0	7.65E−13	7.70E−13	7.65E−13	7.60E−13

TABLE 9: Calculated Rate Constants (in cm^3 molecule^{-1} s^{-1}) for the Second Primary-Site Deuterium Abstraction Reaction

T (K)	$k_{3.2}$(D)	$k_{4.2}$(D)	$k_{5.2}$(D)	$k_{6.2}$(D)
295.0	1.29E−14	1.16E−14	1.32E−14	1.24E−14
351.5	2.47E−14	2.27E−14	2.50E−14	2.41E−14
437.2	5.35E−13	5.00E−13	5.17E−13	5.00E−13
505.0	8.75E−13	8.30E−13	8.50E−13	8.23E−13
603.0	1.57E−13	1.50E−13	1.66E−13	1.62E−13
728.0	2.86E−13	2.76E−13	2.98E−13	2.65E−13
854.0	4.68E−13	4.54E−13	4.82E−13	4.37E−13

TABLE 10: Calculated Rate Constants (in cm^3 molecule^{-1} s^{-1}) for the Secondary-Site Hydrogen Abstraction Reaction

T (K)	$k_{1.3}$(H)	$k_{3.3}$(H)	$k_{5.3}$(H)
295.0	3.70E−13	3.51E−13	2.94E−13
351.5	5.15E−13	5.25E−13	4.43E−13
437.2	8.35E−13	8.10E−13	7.30E−13
505.0	1.09E−12	1.12E−12	1.01E−12
603.0	1.59E−12	1.65E−12	1.49E−12
728.0	2.39E−12	2.50E−12	2.26E−12
854.0	3.34E−12	3.58E−12	3.22E−12

TABLE 11: Calculated Rate Constants (in cm^3 molecule^{-1} s^{-1}) for the Secondary-Site Deuterium Abstraction Reaction

T (K)	$k_{2.3}$(D)	$k_{4.3}$(D)	$k_{5.3}$(D)
295.0	1.41E−13	1.36E−13	1.42E−13
351.5	2.37E−13	2.30E−13	2.39E−13
437.2	4.39E−13	4.29E−13	4.44E−13
505.0	6.50E−13	6.40E−13	6.60E−13
603.0	1.05E−12	1.03E−12	1.06E−12
728.0	1.68E−12	1.66E−12	1.74E−12
854.0	2.56E−12	2.52E−12	2.63E−12

is an average of $k_{1.3}$, $k_{3.3}$, and $k_{5.3}$. Kinetic isotope effects computed from these average values are compared with the results from ref 18 in Tables 18 and 19, and the calculated branching percentages for the OH + C_3H_8 reaction, as calculated from these average values, are compared with experimental values in Table 20. This is about the best we can do as far as comparing to experiment since experimentally these various rates we average were assumed to be the same.

4. Detailed Aspects of Results and Discussion

Reactants and Products Geometry. The geometries calculated at the MP2/aug-cc-pVDZ and MP2−SAC/BTZ levels are very similar. The differences in bond lengths are only about 0.006−0.01 Å, and the differences in bond angles in most cases are within 1°. In the rest of the paper we discuss MP2 geometry unless otherwise stated. In both calculations, the optimized structure of propane has a C_{2v} symmetry and that of isopropyl radical has a C_s symmetry. The secondary hydrogens, H4 and H5 in Figure 1, have the longest C−H bond length, which is correlated to their higher reactivity. The structure of the *n*-propyl radical has C_1 symmetry. On passing from propane to *n*-propyl radical, the bond angle C2−C1−H1 changed from 111.7° to 121.1°, the average primary C−H bond length decreases by more than 0.01 Å, and the C1−C2 bond length decreases by more than 0.03 Å. On passing from propane to isopropyl radical, the bond angle C1−C2−H4 changes from 109.5° to 118.7°, the average secondary C−H bond length decreases by more than 0.01 Å, and both the C1−C2 and the C2−C3 bond lengths decrease by more than 0.03 Å.

Transition-State Geometries. Figure 5 shows the trans transition state for the primary hydrogen abstraction. The transition state is early, and the only significant change in geometry is in the C1−H1 bond length which increases from 1.10 to 1.18 Å. The picture is similar for the gauche primary-site transition state in Figure 6; however, the gauche transition-state is slightly earlier in that there is less elongation of the C1−H3 bond, and the O−H3 bond distance in Figure 6 is longer than the O−H1 distance in Figure 4. The secondary-site transition state (Figure 4) is earlier than either primary-site transition state in that that the C2−H4 distance increases by less than 0.07 Å and the O−H4 distance is longer than the corresponding O−H bonds in the other two transition states by 0.03−0.04 Å. These observations correlate well, according to Hammond's postulate,[38] with the calculated exoergicities and barrier heights in Tables 4 and 5, i.e., the more exoergic reaction (the isopropyl reaction) tends to have a lower barrier and an earlier transition state; and conversely, a higher barrier reaction (the first primary-site reaction) tends to be associated with a later transition state.

Location of the Dynamical Bottleneck. An advantage of the dual-level technique employed here is that it permits a full search along the reaction path for the maximum in the free energy of activation profile as a function of the reaction coordinate s at each temperature T. The deviation of the rate constant k^{CVT} calculated by canonical variational theory from the rate constant k^{TST} calculated by conventional transition-state theory provides a measure of the importance of this search. Table 14 shows the comparison for the perprotio and perdeuterio reactions at three temperatures. The CVT rates are factors of 2−3 lower than the TST ones for C_3H_8 and 10−30% lower than TST for C_3D_8. Thus the kinetic isotope effect (KIE) is very sensitive to the variational effect, decreasing by a factor of 2.0 when the variational transition state is optimized for each case. The k_1/k_6 KIE calculated at three levels of theory is also compared to experiment in Table 14. This table shows that variational transition-state theory agrees with experiment much better than conventional transition-state theory does. This is significant because the classical barrier height cancels out for KIEs in conventional TST and partly cancels in the higher-level dynamical theories. Thus KIEs are often considered the best test of transition-state structure and frequencies.

The variational transition-state location is illustrated in Figure 13 for one of the cases, namely the secondary abstraction reaction of perprotio propane. The first vertical line shows the location of the saddle point, and the other vertical lines show the locations of the variational transition states for 854 and 295 K, i.e., the locations of the free energy of activation profiles[2] at these temperatures. The figure also shows the vibrationally

TABLE 12: Calculated and Experimental Rate Constants (in 10^{-12} cm^3 molecule^{-1} s^{-1}) for R1−R6

	k_1		k_2		k_3		k_4		k_5		k_6	
T (K)	calc	expt	calc	expt	calc	expt	calc	expt	calc	expt	calc	expt
293.0	1.08	1.10	0.65		0.90		0.48		0.65		0.34	
295.0	1.09		0.67	0.61	0.91	0.98	0.49	0.48	0.66	0.83	0.35	0.41
328.5	1.36		0.89	0.80	1.18	1.28	0.67	0.62	0.86	1.00	0.49	0.53
342.0	1.49	1.52	0.99		1.30		0.75		0.95		0.56	
351.5	1.59	1.61	1.07		1.39		0.81		1.02		0.61	
376.2	1.87		1.28	1.20	1.57	1.62	0.98	0.95	1.21	1.37	0.76	0.75
401.0	2.15	2.14	1.51		1.83		1.18		1.41		0.91	
428.0	2.50	2.49	1.79		2.14		1.41		1.66		1.11	
437.2	2.63		1.90	1.72	2.25	2.17	1.50	1.38	1.76	1.79	1.18	1.09
491.0	3.32	3.24	2.57		2.97		2.05		2.34		1.67	
503.5	3.53		2.73	2.47	3.15	2.88	2.20	2.46	2.50	2.46	1.80	1.50
505.0	3.56	3.34	2.75		3.18		2.22		2.52		1.82	
603.0	5.32	4.84	4.31	3.79	4.85	4.19	3.61	3.13	3.96	3.55	3.09	2.55
728.0	8.15		6.88		7.58	6.20	5.89	4.93	6.34	5.31	5.18	
732.0	8.28	7.28	6.97	5.92	7.67		5.99		6.43		5.27	4.25
840.0	11.3		9.96		10.7		8.67	6.60	9.07	6.78	7.76	
854.0	11.8	9.31	10.4	7.86	11.2	8.06	9.05		9.45		8.12	5.88

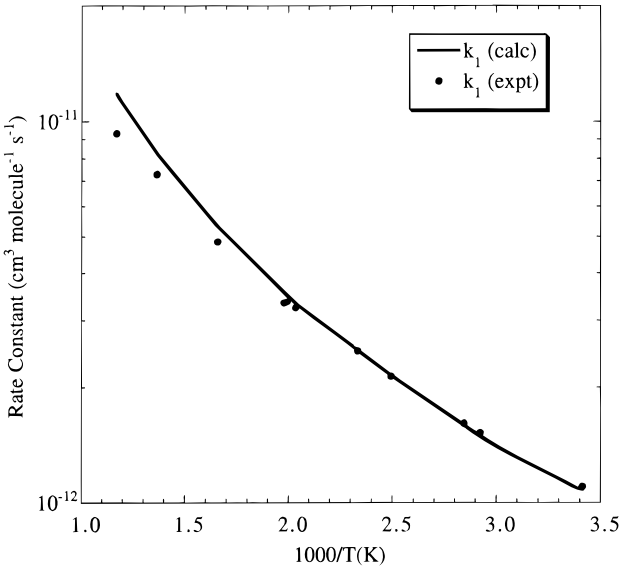

Figure 7. Arrhenius plot of the calculated and experimental rate constants of reaction R1.

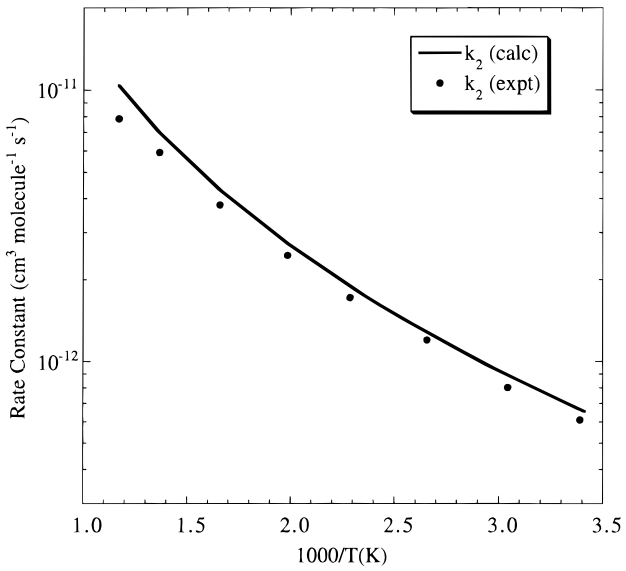

Figure 8. Arrhenius plot of the calculated and experimental rate constants of reaction R2.

adiabatic ground-state potential curve, $V_a^G(s)$, which is equal to the Born−Oppenheimer potential energy along the MEP, $V_{MEP}(s)$, plus the local zero-point energy. The values of $V_a^G(s)$ and $V_{MEP}(s)$ are 70.53 and 0.00 kcal/mol at reactants and 49.47 and −19.60 kcal/mol at products. The maximum of $V_a^G(s)$, which corresponds to the maximum of the free energy of activation profile at 0 K, occurs at $s = -0.43\ a_0$, where it is 71.96 kcal/mol and where $V_{MEP}(s)$ is 1.57 kcal/mol, as compared to 70.69 and 2.20 kcal/mol at the saddle point.

Nature of the Tunneling Process. As discussed elsewhere,[8,39,40] an approximate least-imaginary-action principle is used to select the tunneling method that gives the larger tunneling probabilities. For these reactions, in most cases, the small-curvature assumption[33] leads to larger tunneling probabilities than the large-curvature one, although the large-curvature process does dominate in some cases for the trans primary-site abstraction.

We note that abstraction at the secondary site has a very low barrier and there is actually a greater net effect of tunneling for D abstraction than for H abstraction (see Table 17). In fact, for the H case, nonclassical reflection can actually dominate tunneling (see Table 14). This effect (tunneling *decreasing* the KIE) could never be predicted correctly by a one-dimensional tunneling model that uses the same effective potential barrier for H and D abstraction, but it can arise very naturally in VTST, and in fact it has now been observed in several reactions with low barriers.[41] For such reactions the effective potential for abstracting H is typically lower and broader than the effective potential for abstracting D so that tunneling may be more important for D, despite the greater mass of the transferred particle.

Rate Constants. Tables 6−11 show that at a given temperature the two primary-site abstraction rates are almost the same (within ∼20% for H and ∼10% for D) in the various reactions. The secondary-site abstraction rates are significantly higher due to the lower barrier, and they are also almost constant in the different reactions at a given temperature. The trans primary-site abstraction shows a stronger positive temperature dependence because of a higher barrier, and the trans rate constants at higher temperature are about 20% higher than for the gauche primary-site reaction. The current study thus provides strong support for the assumption by the experimentalists[18,42,43] that the reactivities of primary and secondary sites are separable. However, the three primary hydrogens are not equivalent in the abstraction reaction, and they show slightly different dynamical behaviors.

Table 12 and Figure 7 show good agreement between the experimental and calculated rate constants. The experimental

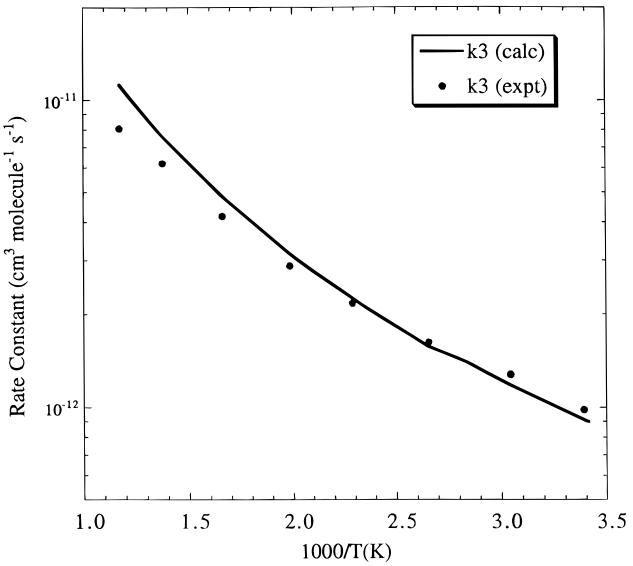

Figure 9. Arrhenius plot of the calculated and experimental rate constants of reaction R3.

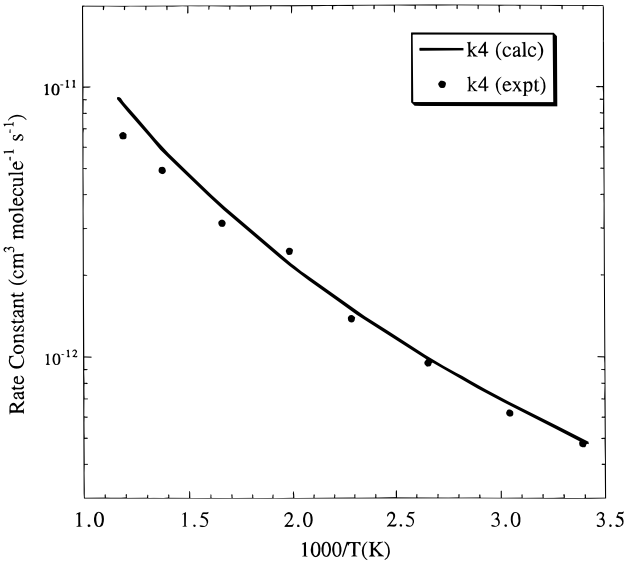

Figure 10. Arrhenius plot of the calculated and experimental rate constants of reaction R4.

values are directly measured rates while the theoretical values are obtained by summing the elementary reaction rates as specified in eqs 12−17. The predicted rates are too high at higher temperatures, which is a common occurrence. This could be due to recrossing effects not accounted for by CVT, an underestimate of the barrier height, or overestimated low-frequency vibrational partition functions (the anharmonicity) in the transition states. Most likely a combination of factors contributes.

Kinetic Isotope Effects (KIEs). In Tables 15 and 16 the calculated KIEs, defined as k_H/k_D, from the averaged values of the calculated primary and secondary abstraction rates are compared with the assumption used by the experimentalists (primany H abstraction KIEs) and with their deduced values (secondary H abstraction KIEs). In the primany abstraction case, the calculated values are slightly higher, while in the secondary abstraction case the calculated result is a little bit lower. In general, the agreement is very good (within 20%), and this validates the experimental assumption of using OH + ethane KIE data.

The KIEs are significantly higher for the primary reaction at low temperature. As in many previously studied cases,[10,12,14]

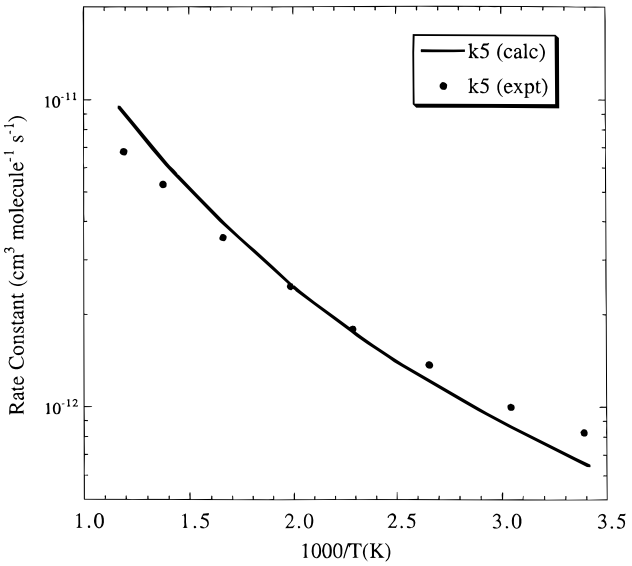

Figure 11. Arrhenius plot of the calculated and experimental rate constants of reaction R5.

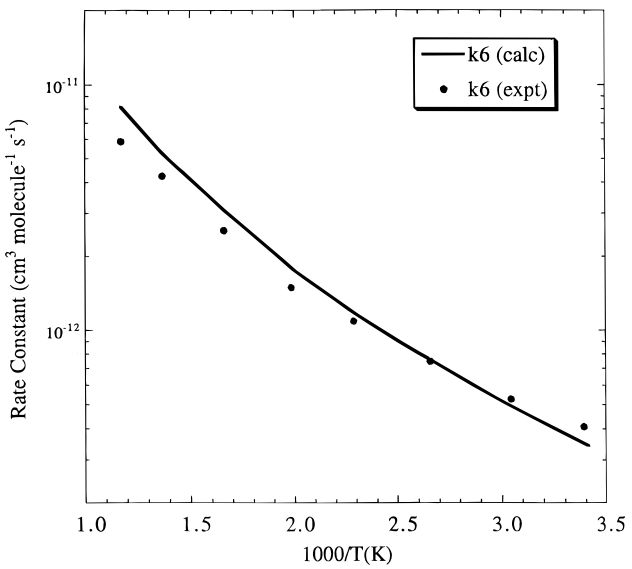

Figure 12. Arrhenius plot of the calculated and experimental rate constants of reaction R6.

TABLE 13: Comparison of CVT/μOMT Kinetic Isotope Effects to Experiment[a]

T (K)	k_1/k_2	k_1/k_3	k_1/k_4	k_1/k_5	k_1/k_6
295.0	1.6	1.2	2.2	1.7	3.1
	1.9	1.2	2.3	1.4	2.8
437.2	1.4	1.2	1.8	1.5	2.2
	1.5	1.2	1.8	1.4	2.4
603.0	1.2	1.1	1.5	1.3	1.7
	1.4	1.2	1.5	1.4	2.0
854.0	1.1	1.1	1.3	1.2	1.5
	1.2	1.2	1.3	1.3	1.6

[a] Upper value: theory. Lower value: experiment (computed from fits of the form $AT^B e^{-C/RT}$ given in ref 18.

the vibrational partition functions provide the main contribution to the KIEs of hydrogen abstraction reactions. The breaking of a C−H bond always results in a normal kinetic isotope effect because the decrease in the C−H vibrational frequency from the reactant to the transition state is much greater than in the C−D case. However, this only explains the "normal" (i.e., greater than unity) kinetic isotope effects observed in the abstraction reactions under study. Why do the primary-site

TABLE 14: Rate Constants (in cm^3 molecule^{-1} s^{-1}), Including Symmetry Numbers, Branching Ratios for H and D (% Primary for R1 and R6), and Kinetic Isotope Effects Calculated at Three Levels of Theory

T (K)		$2k_{1.1}$	$4k_{1.2}$	$2k_{1.3}$	primary % (R1)	$2k_{6.1}$	$4k_{6.1}$	$2k_{6.3}$	primary % (R6)	k_1/k_6
295	TST	7.4E−14	2.1E−13	1.6E−12	15	1.1E−14	3.2E−14	2.8E−13	13	5.8
	CVT	3.0E−14	1.2E−13	5.3E−13	22	9.6E−15	2.8E−14	1.9E−13	17	3.0
	CVT/μOMT	1.1E−13	2.5E−13	7.4E−13	33	1.6E−14	5.0E−14	2.9E−13	19	3.1
	expt[a]									2.8
603	TST	7.9E−13	1.4E−12	5.2E−12	30	3.1E−13	5.6E−13	2.3E−12	27	2.3
	CVT	5.7E−13	1.2E−12	3.3E−12	35	3.0E−13	5.2E−13	2.0E−12	29	1.8
	CVT/μOMT	7.9E−13	1.4E−12	3.2E−12	41	3.2E−13	6.5E−13	2.2E−12	31	1.7
	expt[a]									2.0
854	TST	2.2E−12	3.4E−12	1.0E−11	36	1.1E−12	1.8E−12	5.7E−12	34	1.8
	CVT	1.7E−12	3.1E−12	7.1E−12	40	1.1E−12	1.6E−12	5.1E−12	35	1.5
	CVT/μOMT	2.0E−12	3.1E−12	6.7E−12	43	1.1E−12	1.8E−12	5.3E−12	35	1.4
	expt[a]									1.6

[a] Reference 18 (computed from fits).

TABLE 15: Kinetic Isotope Effects[a] of the Trans Primary-Site Reaction Calculated with Three Levels of Theory

T (K)	TST	CVT	CVT/μOMT
295.0	6.57	3.11	6.56
328.5	5.41	2.84	5.44
351.5	4.88	2.69	4.88
376.5	4.41	2.55	4.38
437.2	3.59	2.31	3.63
505.0	3.03	2.10	2.95
603.0	2.53	1.89	2.43
728.0	2.17	1.70	2.06
854.0	1.94	1.59	1.83

[a] Ratio between the perprotic and the perdeuterated reaction rate constants.

TABLE 16: Kinetic Isotope Effects[a] of the Gauche Primary-Site Reaction Calculated with Three Levels of Theory

T (K)	TST	CVT	CVT/μOMT
295.0	6.58	4.36	4.95
328.5	5.47	3.82	4.26
351.5	4.90	3.56	3.90
376.5	4.41	3.32	3.59
437.2	3.60	2.88	3.13
505.0	3.02	2.48	2.71
603.0	2.53	2.31	2.09
728.0	2.15	2.22	1.93
854.0	1.92	1.99	1.75

[a] Ratio between the perprotic and the perdeuterated reaction rate constants.

TABLE 17: Kinetic Isotope Effects[a] of the Secondary-Site Reaction Calculated with Three Levels of Theory

T (K)	TST	CVT	CVT/μOMT
295.0	5.63	2.73	2.61
328.5	4.72	2.50	2.27
351.5	4.25	2.37	2.15
376.5	3.86	2.25	2.06
437.2	3.18	2.02	1.88
505.0	2.71	1.85	1.64
603.0	2.28	1.66	1.50
728.0	1.96	1.51	1.38
854.0	1.76	1.40	1.27

[a] Ratio between the perprotic and the perdeuterated reaction rate constants.

reactions have KIEs much higher than the secondary-site reaction? A close inspection shows that the tunneling effects are responsible for this difference. The primary-site reactions have higher barriers and thus more tunneling, and in these reactions hydrogens tunnel more easily than deuterium. Thus the primary-site reactions have KIEs almost twice the values of the secondary-site reaction at low temperatures. Specifically, at 295 K in the perprotic reaction, the rate constant of the first primary-site hydrogen abstraction calculated with the tunneling (μOMT) correction is 3.6 times larger than the VTST rate (CVT) without tunneling. This factor is 2.1 for the second primary-site and 1.4 for the secondary-site reaction. For the perdeuterated reactions, this factor is 1.7, 1.8, and 1.5 for the first primary-site, second primary-site, and the secondary-site reaction, respectively.

In Tables 15−17 one can see that in most cases, the KIEs calculated by CVT rate constants are significantly smaller than calculated by TST. This is because the hydrogen reactions show

TABLE 18: Comparison of the Experimental and Calculated (Average) Values of the Primary-Site Abstraction Rates (in cm^3 molecule^{-1} s^{-1}) and the Kinetic Isotope Effects

T (K)	k_H^P(calc)	k_D^P(calc)	KIE(calc)	k_H^P(exp)	k_D^P(exp)	KIE(exp)
295	1.80E−13	3.08E−14	5.85	1.55E−13	3.27E−14	4.74
328.5	2.40E−13	4.38E−14	4.97	2.18E−13	5.38E−14	4.05
376.5	3.43E−13	8.29E−14	4.13	3.33E−13	9.79E−14	3.40
437.2	5.02E−13	1.46E−13	3.44	5.16E−13	1.80E−13	2.87
503.5	7.13E−13	2.48E−13	2.88	2.79E−13	3.17E−13	2.50
603	1.13E−12	4.83E−13	2.34	1.17E−12	5.45E−13	2.15
732	1.81E−12	9.20E−13	1.97	1.82E−12	9.65E−13	1.89
854	2.70E−12	1.52E−12	1.77	2.53E−12	1.47E−12	1.72

TABLE 19: Comparison of the Experimental and Calculated (Average) Values of the Secondary-Site Abstraction Rates (in cm^3 molecule^{-1} s^{-1}) and the Kinetic Isotope Effects

T (K)	k_H^S(calc)	k_D^S(calc)	KIE(calc)	k_H^S(exp)	k_D^S(exp)	KIE(exp)
295	6.77E−13	2.79E−13	2.42	7.81E−13	2.99E−13	2.61
328.5	8.48E−13	3.85E−13	2.20	9.41E−13	3.68E−13	2.56
376.5	1.13E−12	5.73E−13	1.98	1.19E−12	5.33E−13	2.23
437.2	1.58E−12	8.75E−13	1.81	1.46E−12	7.05E−13	2.07
503.5	2.13E−12	1.29E−12	1.65	1.80E−12	8.67E−13	2.08
603	3.15E−12	2.09E−12	1.51	2.47E−12	1.44E−12	1.72
732	4.83E−12	3.44E−12	1.41	3.33E−12	2.24E−12	1.49
854	6.76E−12	5.14E−12	1.32	4.20E−12	2.92E−12	1.44

TABLE 20: Calculated and Experimental Values of the Percentage of Primary Abstractions for the OH+ C_3H_8 Reaction

T (K)	present	expt[a]
295	32	21−29
328.5	34.5	26−33
376.5	36	33−38
437.2	36	40−42
503.5	39	46−47
603	40	49−53.5
732	41	52−59
854	43	55−63

[a] Range of results obtained from three experimental studies.[18,42,43]

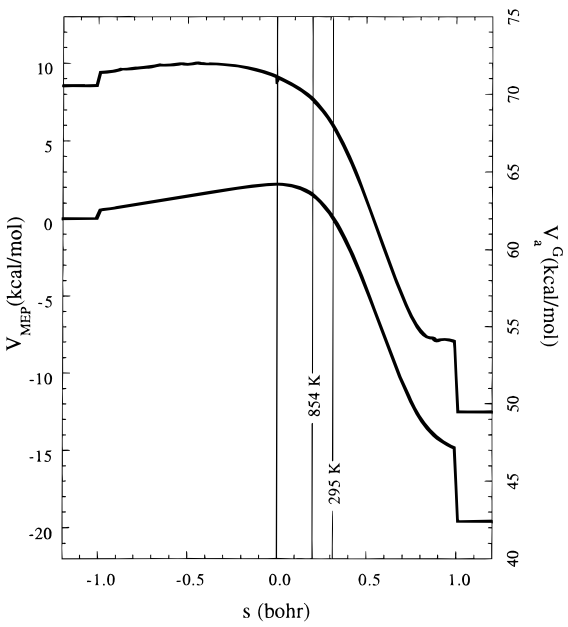

Figure 13. Vibrationally adiabatic ground-state potential curve, $V_a^G(s)$, with scale at right, and the Born−Oppenheimer potential energy along the MEP, $V_{MEP}(s)$, with scale at left, as functions of the reaction coordinate s for the abstraction of a secondary H from perprotio propane by OH. The vertical line at $s = 0.20\ a_0$ is the location of the variational transition state at 854 K, and the vertical line at $s = 0.31\ a_0$ is the location of the variational transition state at 295 K. The flat sections at the ends of the curves indicate their asymptotic values.

much stronger variational effects at lower temperatures. The tunneling correction increases the KIEs for the primary-site reactions, especially for the first one, but it decreases the KIEs slightly for the secondary-site reaction.

Table 13 compares theory to experiment for the observable KIEs. The calculations very faithfully reproduce all the experimental trends, and the overall quantitative agreement with experiment is quite gratifying. Table 12 shows that all five kinetic isotope effects are in good agreement with experiment.

Branching Ratios. As seen in Table 20, the calculated branching ratios of the perprotic reaction are significantly different from the values inferred from previous experimental[18,42,43] studies at higher temperatures. This results from the fact that the calculated secondary-site abstraction rates have much stronger temperature dependence than the experimental values (see Tables 6−11). This may due to the more anharmonic nature of the hindered-rotor mode in the secondary-site transition state since the harmonic frequency is only 22.7 cm^{-1}, which is only about half of the values at the two primary-site transition states, 40.7 and 58.5 cm^{-1}, respectively.

Hindered Rotator Treatment. As mentioned in section 2, we estimated the barrier to internal rotation by ab initio calculations. In particular we carried out such calculations by the MP2−SAC method. Table 21 gives the harmonic frequencies for the torsion, the internal-rotation barrier predicted from these frequencies by the original hindered-rotator model, the SAC internal rotational barrier, the reduced moment of inertia (with symmetry number equal to unity), and the calculated vibrational partition functions at two temperatures. We see that the hindered-rotator correction with the original method is almost negligible at 293 K and never more than 24% at 845 K, whereas with the improved method it lowers the transition-state partition function by 26−27% at 293 K and by 49−50% at 854 K.

Substituent Effects. We note that the good agreement with experiment that we achieved for OH + CH_4 in ref 9, for OH + CD_4 and C_2H_6 in ref 10, and for OH + $C_3H_{8-n}D_n$ in the present paper allows us to estimate the classical barrier height in each case. This quantity is not well-known for most reactions because of the difficulty of disentangling zero-point effects, thermal free energy effects, and dynamical effects from the raw potential energy barriers. The estimates obtained from the present series of papers for the three cases are compared in Table 22. It is not clear quite how much confidence we can place in these numbers or whether any systematic errors are in the same directions for the various cases. For example the absolute rate constants we predict for OH + CH_4 agree with experiment only within a factor of 2, and Malick and Petersson[44] have estimated a lower barrier, 5.1 kcal, for that case. Nevertheless, taking our own numbers at face value one can place quantitative values on the substituent effects, namely 2.5 kcal/mol for one methyl substituent, 4 kcal/mol for two methyl substituents, and 3 kcal/mol for an ethyl substituent.

TABLE 21: Data and Partition Functions for Improved Treatment of Hindered Internal Rotation at the Saddle Point of Reaction (R1)

	primary site		
	1	2	secondary site
	Data		
ω_m (cm^{-1})	41	58	23
$\bar{I}_m$ ($10^4\ m_e a_0^2$)	5.25	4.70	4.00
W_m (kcal/mol) [eq 6]	2.27	4.19	0.54
W_m (kcal/mol) [SAC]	0.16	0.16	0.17
	Partition Function (293 K)		
harmonic	4.99	3.47	8.98
eqs 1 and 4	4.98	3.47	8.40
eqs 1 and 11	3.65	2.53	6.68
	Partition Function (854 K)		
harmonic	14.6	12.1	26.2
eqs 1 and 4	14.1	10.1	19.9
eqs 1 and 11	7.4	5.0	13.3

TABLE 22: Classical Barrier Heights for OH Abstraction Reactions

	$V^{\ddagger}$ (kcal/mol)
OH + CH_4	6−7
OH + C_2H_6	4.0
OH + C_3H_8	
in-plane primary T.S.[a]	3.7
out-of-plane primary T.S.	3.2
secondary T.S.	2.2

[a] T.S. ≡ transition state

Errors. The leading sources of error at this point are probably the treatment of vibrations as rectilinear and harmonic and the simplicity of the methods used to interpolate the shape of $V_{MEP}(s)$. Additional work being carried out in our group is designed to eventually allow these sources of potential error to be mitigated.

5. Summary

We have studied the reactions in which a hydroxyl radical abstracts a protium or deuterium atom from propane and five different isotopic analogues of propane. The calculations are based on extended-basis-set electronic structure calculations and dual-level direct dynamics calculation with multidimensional semiclassical tunneling corrections. The MP2/aug-cc-pVDZ calculations agree well with experimental reaction energetics. Scaling all the correlation energy with a balanced basis set, MP2−SAC/BTZ, is applied to correct the calculated correlation energy in both the geometry optimization and barrier height calculations. The scaling of the correlation energy in the SAC method is found to have little effect on the calculated geometries but a larger effect on the calculated barrier heights. Three

distinct transition states are characterized, two for the primary-site reaction and one for the secondary-site reaction. All transition states are "early" in the sense that the propane moiety is only slightly deformed from the reactant geometry. The secondary-site reaction has a lower calculated barrier height, as expected from experimental rate constants.

Dynamics calculations are based on a dual-level approach in which the low-level data are obtained from an AM1−SRP semiempirical surface, which is reparametrized from the original AM1 method using a genetic algorithm to fit the experimental reaction energetics and the MP2−SAC/BTZ barrier heights. The higher level for the dual-level calculation is SB-MP2−SAC/BTZ for the transition-state energy, MP2−SAC/BTZ for the reaction path and energy of reaction, and MP2/aug-cc-pVDZ for vibrational frequencies. SB denotes the use of a single scale factor of 0.85 applied to all three classical barrier heights, which is a small correction, 0.4−0.7 kcal. This level of calculation is then used to predict 22 independent reaction rates which cannot be fully sorted out experimentally, and this allows us to test the assumptions of the experimentalists.

The rate constant calculations show that the assumption of the separability of the abstraction sites is, to a very good approximation, valid. The rate constant per hydrogen atom is almost independent of the isotopic identity of the hydrogens at other sites. After scaling the MP2−SAC barrier heights by a factor of 0.85 to best fit the experimental rates of the perprotic reaction, all the calculated rate constants and kinetic isotope effects, after transforming to experimental observables, are in good agreement with direct or indirect experimental values. The calculations also show clearly that the difference in the kinetic isotope effects between the primary-site and the secondary-site reactions is primarily due to the tunneling effects.

This study demonstrates the power of the dual-level dynamics calculational method. Accurate modeling of the dynamics of a system of this size is extremely difficult because the cost and computer storage of calculations required for reliable electronic structure calculations. The dual-level dynamics method minimizes the amount of high-level ab initio data required by constructing a realistic low-level surface and by interpolating the differences between the two-levels to estimate the high-level values where they are not available. The dual-level method provides a reasonable compromise between accuracy and affordability in reaction dynamics calculations. This opens new possibilities for the accurate modeling of various kinds of complex organic reactions.

Acknowledgment. This work is supported in part by the U.S. Department of Energy, Office of Basic Energy Sciences.

Supporting Information Available: Tables of vibrational frequencies, reduced moments of inertia, and geometries of reactants, products, and transition states (31 pages). This information is available in many libraries since it immediately follows the article in the microfilm version of the Journal. See any current masthead page for ordering information and Internet access instructions.

References and Notes

(1) Truhlar, D. G.; Garrett, B. C. *Acc. Chem. Res*. **1980**, *13*, 440.

(2) Truhlar, D. G.; Isaacson, A. D.; Garrett, B. C. In *Theory of Chemical Reaction Dynamics*; Baer, M., Ed.; CRC Press: Boca Raton, FL, 1985; Vol. 4, p 65.

(3) Truhlar, D. G.; Garrett, B. C. *Annu. Rev. Phys. Chem.* **1984**, *35*, 159.

(4) Truhlar, D. G.; Steckler, R.; Gordon, M. S. *Chem. Rev. (Washington, D.C.)* **1987**, *87*, 217. Schatz, G. C. *Rev. Mod. Phys*. **1989**, *61*, 669.

(5) Gonzalez-Lafont, A.; Truong, T. N.; Truhlar, D. G. *J. Phys. Chem*. **1991**, *95*, 4618.

(6) Viggiano, A. A.; Paschkewitz, J.; Morris, R. A.; Paulson, J. F.; Gonzalez-Lafont, A.; Truhlar, D. G. *J. Am. Chem. Soc*. **1991**, *113*, 9404.

(7) Gonzalez-Lafont, A.; Truong, T. N.; Truhlar, D. G. *J. Chem. Phys.* **1991**, *95*, 8875.

(8) Liu, Y.-P.; Lu, D.-h.; Gonzalez-Lafont, A.; Truhlar, D. G.; Garrett, B. C. *J. Am. Chem. Soc*. **1993**, *115*, 7806.

(9) Melissas V. S.; Truhlar, D. G. *J. Chem. Phys.* **1993**, *99*, 1013.

(10) Melissas V. S.; Truhlar, D. G. *J. Chem. Phys.* **1993**, *99*, 3542. Melissas V. S.; Truhlar, D. G. *J. Phys. Chem.* **1994**, *98*, 875.

(11) Hu, W.-P.; Liu, Y.-P.; Truhlar, D. G. *J. Chem. Soc., Faraday Trans.* **1994**, *90*, 1715.

(12) Corchado, J. C.; Espinosa-Garcia, J.; Hu, W.-P.; Rossi, I.; Truhlar, D. G. *J. Phys. Chem*. **1995**, *99*, 4618.

(13) Hu, W.-P.; Truhlar, D. G. *J. Am. Chem. Soc*. **1995**, *117*, 10726.

(14) Hu, W.-P.; Truhlar, D. G. *J. Am. Chem. Soc*. **1996**, *118*, 860.

(15) Gordon, M. S.; Truhlar, D. G. *J. Am. Chem. Soc*. **1986**, *108*, 5412. Truong, T. N.; Truhlar, D. G.; Baldridge, K. K.; Gordon, M. S.; Steckler, R. *J. Chem. Phys*. **1989**, *90*, 7137. Gordon, M. S.; Nguyen, K. A.; Truhlar, D. G. *J. Phys. Chem*. **1989**, *93*, 7356. Rossi, I.; Truhlar, D. G. *Chem. Phys. Lett*. **1995**, *234*, 64.

(16) Chase, M. W., Jr.; Davies, C. A.; Downey, J. R., Jr.; Frurip, D. J.; McDonald, R. A.; Syverud, A. N. *J. Phys. Chem. Ref. Data* **1985**, *14*, Suppl. 1.

(17) Hehre, W. J.; Radom, L.; Schleyer, P.v. R.; Pople, J. A. *Ab initio Molecular Orbital Theory*; Wiley: New York, 1986.

(18) Droege, A. T.; Tully, F. P. *J. Phys. Chem.* **1986**, *90*, 1949.

(19) Tully, F. P.; Droege, A. T.; Koszykowski, M. L.; Melius, C. F. *J. Phys. Chem.* **1986**, *90*, 691.

(20) Brown, F. B.; Truhlar, D. G. *Chem. Phys. Lett*. **1985**, *117*, 307.

(21) Dunning, T. H., Jr. *J. Chem. Phys.* **1989**, *90*, 1007.

(22) Kendall, R. A.; Dunning, T. H. Jr.; Harrison, R. J. *J. Chem. Phys.* **1992**, *96*, 6796.

(23) Pople, J. A.; Santry, D. P.; Segal, G. A. *J. Chem. Phys.* **1965**, *43*, S129.

(24) Dewar, M. J. S.; Zoebisch, E. G.; Healy, E. F.; Stewart, J. J. P. *J. Am. Chem. Soc.* **1985**, *107*, 3902.

(25) Stewart, J. J. P. *J. Comput. Chem.* **1989**, *10*, 221.

(26) Rayez, M. T.; Rayez, J.-C.; Bérces, T.; Lendvay, G. *J. Phys. Chem*. **1993**, *97*, 5570.

(27) Bash, P.; Ho, L. L.; Mackerell, A. D.; Levine, D.; Hallstrom, P. *Proc. Natl. Acad. Sci. U.S.A.* **1996**, *93*, 3698.

(28) Rossi, I.; Truhlar, D. G. *Chem. Phys. Lett.* **1995**, *233*, 231.

(29) Quantum Chemistry Program Exchange program no. 597: Baker, J.; Jensen, F.; Rzepa, H. S.; Stebbings, A. *QCPE Bull*. **1990**, *10*, 91.

(30) Isaacson, A. D.; Truhlar, D. G. J. *Chem. Phys*. **1982**, *76*, 1380.

(31) Garrett, B. C.; Truhlar, D. G. *J. Phys. Chem*. **1979**, *83*, 2921. Skodje, R. T.; Truhlar, D. G.; Garrett, B. C. *J. Chem. Phys*. **1982**, *77*, 5955.

(32) Truhlar, D. G. *J. Comput. Chem.* **1991**, *12*, 266.

(33) Lu, D.-h.; Truong, T. N.; Melissas, V. S.; Lynch, G. C.; Liu, Y.-P.; Garrett, B. C.; Steckler, R.; Isaacson, A. D.; Rai, S. N.; Hancock, G. C.; Lauderdale, J. G.; Joseph, T.; Truhlar, D. G. *Comput. Phys. Commun*. **1992**, *71*, 235.

(34) *JANAF Thermochemical Tables*, 3rd ed.; Chase, M. W., Jr.; Davies, C. A., Downey, J. R., Jr.; Frurip, D. J., McDonald, R. A., Syverud, A. N., Eds.; Natl. Stand. Ref. Data Ser., Natl. Bur. Stand.: Washington, DC, 1985; Vol. 14.

(35) GAUSSIAN 92, Revision G.1: Frisch, M. J.; Trucks, G. W.; Schlegel, H. B.; Gill, P. M. W.; Johnson, B. G.; Wong, M. W.; Foresman, J. B.; Robb M. A.; Head-Gordon, M.; Replogle, E. S.; Gomperts, R.; Andres, J. L.; Raghavachari, K.; Binkley, J. S.; Gonzalez, C.; Martin, R. L.; Fox, D. J.; Defrees, D. J.; Baker, J.; Stewart, J. J. P; Pople, J. A. Gaussian, Inc.: Pittsburgh, PA, 1993.

(36) Stewart, J. J. P. *J. Comput.-Aided Mol. Design* **1990**, *4*, 1.

(37) Hu, W.-P.; Lynch, G. C.; Liu, Y.-P.; Truong, T. N.; Rossi, I.; Stewart, J. J. P; Steckler, R.; Garrett, B. C.; Isaacson A. D.; Gonzalez-Lafont, A.; Lu, D.-H.; Melissas, V.; Rai, S. N.; Hancock, G. C.; Joseph, T.; Truhlar, D. G. Morate version 6.3/P6.3-M5.05, University of Minnesota, Minneapolis, 1994, unpublished.

(38) Hammond, G. S. *J. Am. Chem. Soc*. **1955**, *77*, 334.

(39) Truhlar, D. G.; Lu, D.-h.; Tucker, S. C.; Zhao, X. G.; Gonzalez-Lafont, A.; Truong, T. N.; Maurice, D.; Liu, Y.-P.; Lynch, G. C. *ACS Symp. Ser*. **1992**, *502*, 16.

(40) Truhlar, D. G. *J. Chem. Soc., Faraday Trans*. **1994**, *90*, 1740.

(41) Truong, T. N.; McCammon, J. A. *J. Am. Chem. Soc*. **1991**, *113*, 7504. Storer, J. W.; Houk, K. N. *J. Am. Chem. Soc*. **1993**, *115*, 10426.

(42) Cohen, N. *Int. J. Chem. Kinet*. **1982**, *14*, 1339.

(43) Walker, R. W. *Int. J. Chem. Kinet*. **1985**, *17*, 573.

(44) Malick, D. K.; Peterson, G. A., to be published.